Natural Hazards (2021) 106:1619–1637
https://doi.org/10.1007/s11069-020-04462-2

ORIGINAL PAPER

Extreme sea levels at Rapa Nui (Easter Island) during intense atmospheric rivers

Matías Carvajal[1,2] · Patricio Winckler[3,4,5] · René Garreaud[6] · Felipe Igualt[7] · Manuel Contreras-López[3] · Pamela Averil[3] · Marco Cisternas[8,2] · Alejandra Gubler[4] · Wolfgang A. Breuer[9]

Received: 27 July 2020 / Accepted: 2 December 2020 / Published online: 2 January 2021

Abstract
In addition to the tsunami hazard posed by distant great earthquakes, Rapa Nui (Easter Island), in the Southeast Pacific Ocean, is exposed to frequent and intense coastal storms. Here, we use sea-level records and field surveys guided by video and photographic footage to show that extreme sea levels at Rapa Nui occur much more frequent than previously thought and thus constitute an unrecognized hazard to the inland's maritime supply chain. We found that extreme sea-level events, including the two most extreme (March 5th and May 5th, 2020) in our 17-month-long analyzed period (from January 1st, 2019, to May 31st, 2020), resulted from constructive superpositions of seiches on the shelf, storm surges and high tides. By further analyzing time series of atmospheric and wind-generated wave data, we conclude that these extreme sea levels are ultimately driven by the breaking of large waves near the coastline (i.e., wave setup), with lesser contribution of barometric setup and even less of wind setup. We also propose that these large waves were mainly generated from strong, long-lasting, NW winds associated with intense atmospheric rivers (long, narrow regions in the atmosphere that transport abundant water vapor) passing over Rapa Nui. Given that the intensity of atmospheric rivers and sea level are thought to increase as climate changes, a deeper understanding of the relation between meteorological and oceanographic processes at Rapa Nui is strongly needed.

Keywords Rapa Nui · Easter Island · Seiches · Meteotsunamis · Storm surge · Sea level · Shelf resonance · Atmospheric rivers · Integrated water vapor

1 Motivation

Isolated in the southeast Pacific Ocean, Rapa Nui, also known as Easter Island (Chile; 27,1°S–109,4°W), is the most remote inhabited place in the world (Fig. 1a). Its triangular-shaped surface of ~ 164 km^2 is home to about 7750 people, most of them living in the village of Hanga Roa (Rangel-Buitrago et al. 2018), on the western coast of the island

✉ Matías Carvajal
matias.carvajal.ramirez@gmail.com

Extended author information available on the last page of the article

(Fig. 1b). The island's main port infrastructure is at Hanga Piko Harbor, located 1 km south of Hanga Roa (Fig. 1b). All maritime cargo arriving on the island is unloaded there with the aid of self-propelled barges that transfer goods from ships anchored offshore. This harbor also hosts the island's only tide gauge station.

The location of Rapa Nui makes it particularly exposed to large tsunamis generated in the far field and to intense coastal storms produced by diverse weather phenomena. Flooding of low-lying areas due to far-field tsunamis has been identified as a greater risk than that from storms (Quillam et al. 2014). This is not surprising since the island is surrounded by the Ring of Fire, where subduction zones trigger the world's greatest megathrust earthquakes (Bilek and Lay 2018) (Fig. 1a). However, coastal storms are much more frequent than far-field tsunamis and can also cause inundation in low-lying areas. Indeed, photographic and video footage published in social media evidence recent flooding episodes at Hanga Roa and Hanga Piko during intense weather conditions. These episodes have attracted the attention of locals and authorities as also causing major impacts on harbor operations and therefore constitute a previously unrecognized hazard to the supply of the island.

Here, we show that extreme sea levels at Rapa Nui occur much more frequent than previously thought and result from constructive superpositions of seiches, storm surges and high tides.

2 Setting

Rapa Nui is the largest emerged part of the Easter Seamount Chain, an E-W trending alignment of volcanic seamounts extending eastward of the East Pacific Rise for about 3000 km (Baker et al. 1974; Rappaport et al. 1997). Due to its volcanic origin, the island of Rapa Nui rises abruptly from abyssal plain depths of ~ 3000 m to typical altitudes of ~ 150 m above sea level (Fig. 1a). As for most volcanic islands, Rapa Nui's shelf is very narrow,

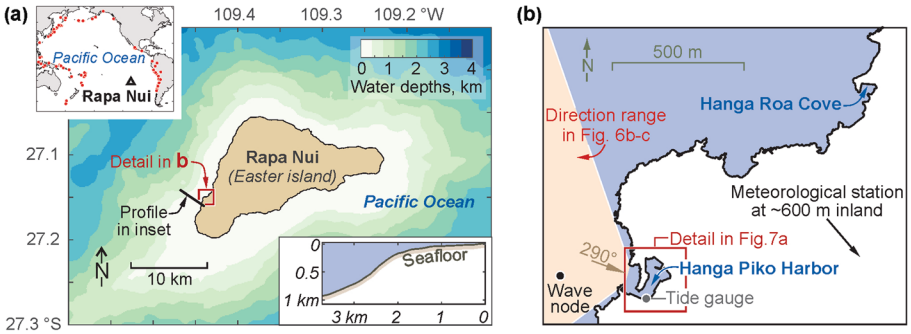

Fig. 1 Index maps. **a** Bathymetry around Rapa Nui (Easter Island). Upper left inset shows the location of Rapa Nui relative to the epicenters (red dots) of global earthquakes greater than magnitude 8 since 1900 (Bilek and Lay 2018). Lower right inset shows a bathymetric profile off Hanga Piko along the track indicated by the black line. **b** Study area showing the Hanga Roa Cove and Hanga Piko Harbor. The pink area represents the direction range (240–340°) in which winds and waves impact directly to the Harbor, with 290° as the pure cross-shore direction. The black dot represents the node where the wave hindcast is obtained, the gray dot shows the tide gauge location, and the black southeastward arrow points to Mataveri Airport, where the meteorological stations is located

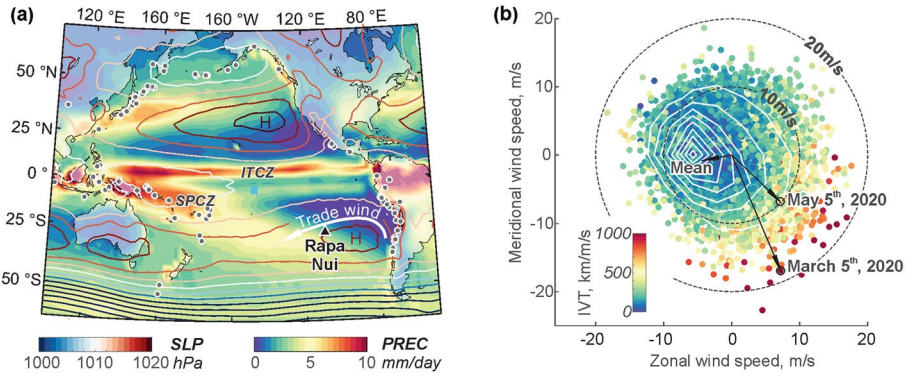

Fig. 2 Climate background of Rapa Nui. **a** The background shading indicates long-term March-April-May mean (1980–2010) rainfall rate (in mm per day). The Intertropical Convergence Zone (ITCZ) and South Pacific Convergence Zone (SPCZ) are indicated. The overlay contours are the long-term seasonal mean sea-level pressure (in hPa). The letter H indicates the centers of the subtropical high-pressure cells over the SE and NE Pacific. The anticyclonic flow around these cells contributes to the trade winds along their equatorward side as indicated by the white arrow passing over Rapa Nui (black triangle). Shading grey dots indicate the epicenters of global earthquakes shown in Fig. 1a. **b** Bivariate distribution of the daily (12:00 UTC) zonal (EW) and meridional (SN) components of the wind at 10 m above sea level for a point at 27 ºS, 109.1 ºW. Data from ERA-5 reanalysis covering the period January 1, 2000–October 7, 2020. White contours indicate density of data points. In this polar plot, each circle can be interpreted as the head of a wind vector. The circles are colored according to the integrated water vapor transport (IVT, scale at bottom) of that day. Also included is the long-term mean wind vector (blowing from the ENE), as well as the wind vectors for March 5th and May 5th, 2020 (blowing from the NNW)

with water depths of hundreds to thousands of meters within a few to several kilometers from the coast (Fig. 1a). Near Hanga Piko, the shelf is about 2 km wide with the seaward edge at about 100 m below sea level (inset in Fig. 1a). Inside the harbor, water depths are of ~ 2 m.

The island is located at the western flank of the southeast Pacific subtropical anticyclone (Fig. 2a) which is maintained by the descending branch of the Hadley cell (e.g., Rahn and Garreaud 2014). During summer–fall, this results in predominant trade (easterly) winds passing over the island as shown in the polar diagram in Fig. 2b, in which each point represents zonal (EW) and meridional (NS) wind components at 10 m above MSL for a given day (12:00 UTC), along with the long-term mean wind vector that is nearly 5 m/s from the east. The weather at Rapa Nui, however, is frequently disrupted by transient systems of both tropical and extratropical origin. The South Pacific Convergence Zone (SPCZ), with copious rainfall and unsettled weather, is rooted in the tropical central Pacific and extends southeastward not far from Rapa Nui (Fig. 2a). Farther south, there is an incessant transit of midlatitude cyclones embedded in the southern hemisphere westerly wind belt (40-55ºS).

Cold fronts, anchored in extratropical cyclones, contribute to the formation of atmospheric rivers (ARs), long filaments of high water vapor transport (e.g., Ralph et al. 2018) that can reach Rapa Nui and transfer vast amounts of moisture from the tropical Pacific into midlatitudes. Indeed, global surveys indicate a local maximum of AR frequency over the subtropical SE Pacific accounting for over 30% of the rainfall accumulation and connected with nearly half of the extreme wind events (Guan and Waliser 2015). ARs often extend for a few thousand kilometers, and they can last 1–3 days over Rapa Nui. During that period,

strong low-level winds blowing from the NW (i.e., opposed to the more prevalent trade winds) account for most of the water vapor transport (IVT).[1] These events stand out in the polar wind diagram (Fig. 2b) by their warm-colored circles (indicating high IVT) in the lower-right quadrant, with speeds typically above 10 m/s. While ARs can produce local precipitation, most of the vapor continues its travel until they make landfall in south-central Chile (Viale et al. 2018).

Ocean tides are characterized by a mixed regime with a maximum range of ~ 0.8 m during spring tides and ~ 0.3 m during neap tides. Mean wave climate is controlled by swells emerging from extratropical cyclones moving on a latitudinal belt between 40°S and 60°S. The associated winds transfer energy to waves, which propagate from the South Pacific Ocean, reaching the island with mean significant wave heights of 2.6 m, mean periods of 9.0 s and mean directions of 211° (Beyá et al. 2017). However, these statistical parameters overshadow the multimodal nature of wave climate in the western coast of the island, where northwestern swells occasionally arrive during summer and locally-generated wind waves regularly arrive in winter.

3 Data and methods

3.1 Recorded and modeled data sets

We examined both atmospheric and sea-level data for a 17-month-long period spanning from January 1st, 2019, to May 31st, 2020 (Fig. 3). The former includes 1-min resolution times series of wind speed, wind direction and atmospheric pressure at sea level, recorded by the meteorological station of the Mataveri Airport, located about 600 m inland of Hanga Piko (Fig. 1b). The sea-level data, also with 1-min resolution obtained by averaging 120 data points per minute (personal communication with former tide gauge chief operator Juan Fierro), was recorded by a tide gauge located in the southeast corner of the Hanga Piko Harbor (Fig. 1b).

Synoptic-scale meteorological conditions were described using hourly fields of sea-level pressure (SLP), winds (zonal and meridional components) at selected levels and integrated water vapor transport (IVT) from the European Center for Weather Forecast reanalysis (ERA5) available from 1979 onwards on a $0.5° \times 0.5°$ latitude–longitude grid (Hersbach et al. 2018). The data providers and accessibility are detailed in the Acknowledgement section.

Given the absence of local observations of wind-generated waves, we modeled wave climate in a node located 300 m off Hanga Piko at a depth of 20 m (see node location in Fig. 1b). To this end, we used Wavewatch III (Tolman, 2014) with parametrizations adjusted for Rapa Nui (Beyá et al., 2017) and wind fields from NOAA's Global Forecast System GFS database. In the wave node, we retrieved statistical wave parameters of significant wave heights, mean directions and mean periods.

[1] The integrated water vapor transport (IVT) is a vector that gauges the flux of moisture through the entire troposphere over a given grid box. Its zonal and meridional components are obtained by the vertical integration of uq and vq, where (u,v) are zonal and meridional wind and q is the water vapor mixing ratio (e.g., Viale et al. 2018).

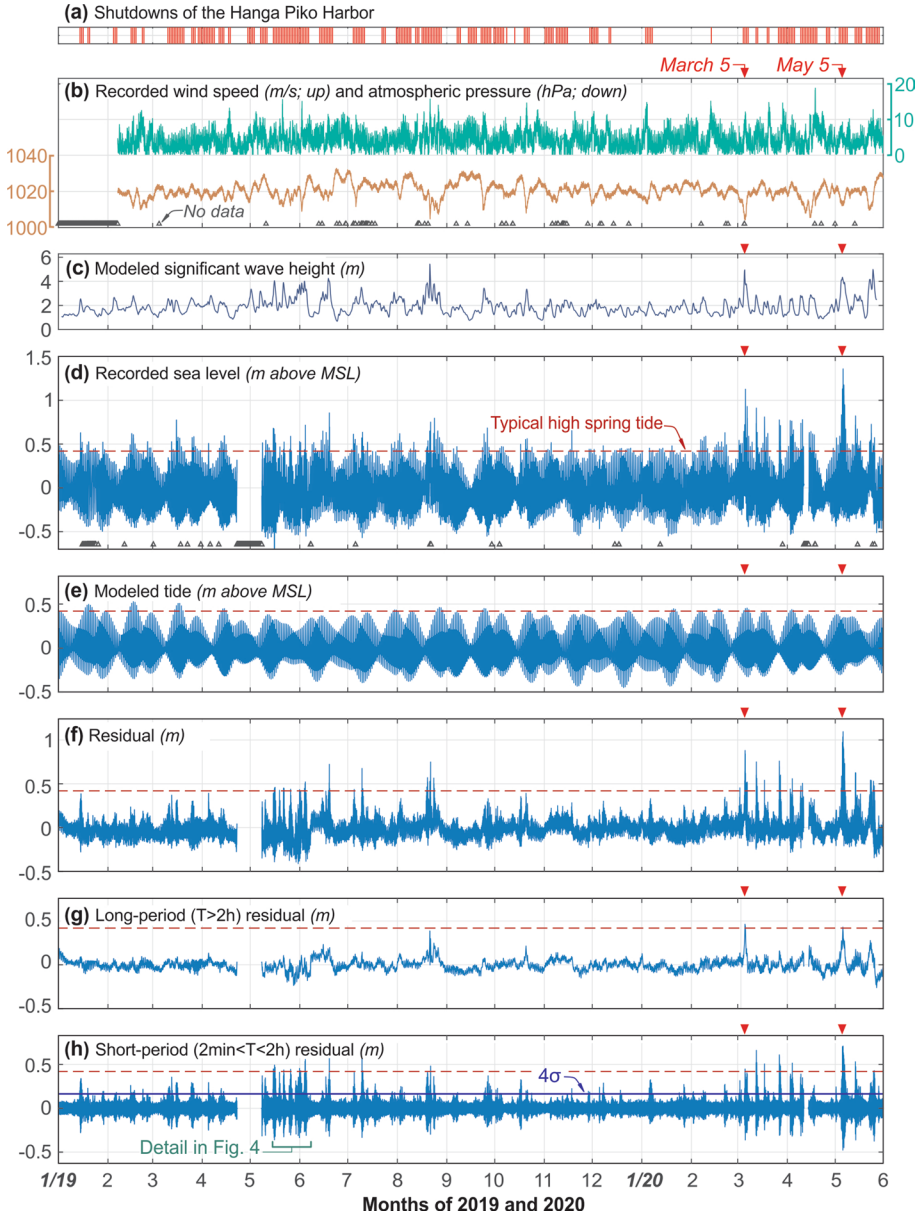

Fig. 3 Main datasets time series used in this study. **a** Shutdowns of the Hanga Piko Harbor (red lines). **b** Recorded wind speed (green) and atmospheric pressure (orange) at Mataveri Airport (See Fig. 1b for station location). **c** Modeled significant wave height at a node located 300 m off Hanga Piko at 20 m water depths (see Fig. 1b for node location). **d** Recorded sea level at Hanga Piko's tide gauge. **e)** Modeled astronomical tide. **f** Residual sea level. **g–h** Long- and short-period component of the residual sea level, respectively. Blue horizontal line in (h) indicates four standard deviations (4σ) from the mean, used as a threshold for meteotsunamis identification (Monserrat et al. 2006). All time series span from January 1st, 2019, to May 31st, 2020 (17 months). Red downward triangles indicate the March 5th and May 5th, 2020, extreme sea-level events analyzed in this study. The upward black triangles in **b** and **d** indicate positions of data gaps

3.2 Time series analyses

Each recorded data set was first subjected to careful quality control, in which outliers were removed, gaps were identified and data offsets were adjusted. Tidal oscillations in the sea-level data were modeled (Fig. 3e) using the T_tide software package based on harmonic analysis (Pawlowicz et al., 2002) and then removed from the recorded sea level to obtain the residual sea level (Fig. 3f).

We decomposed the atmospheric and residual sea-level time series into long-period signals with periods longer than 2 h (Fig. 3g) and short-period signals with periods between 2 min (Nyquist period) and 2 h (Fig. 3h). This decomposition yields sea-level signals that reflect different meteorological and oceanographic processes: While the long-period signal includes the storm surge and other lower-frequency anomalies, the short-period signal is expected to comprise different classes of oscillations in the tsunami frequency band (i.e., ~ 2 min to 2 h). The spectral separation was made using the wavelet method described by Torrence and Compo (1998) with the bias corrections introduced by Liu et al. (2007). In particular, we first obtained the long-period signals by applying a low-pass wavelet filter with a cutoff period of 2 h to the recorded atmospheric and residual sea-level time series. The short-period signals were then obtained by subtracting these resulting long-period signals from the parent time series. We remark that the resulting short-period signal of the sea level may contain infragravity (IG) waves with periods over 2 min, as well as aliased IG waves with shorter periods, but excludes waves with typical periods between 2 and 30 s.

3.3 Field survey guided by visual records

To gain insights on the effects of extreme sea-level events at the coast, we conducted both remote and in situ field surveys guided by both video and photographic footage obtained from eyewitnesses during the March 5th and May 5th (2020) events, when the recorded sea level reached the highest values in our analyzed period (Fig. 3d). Our survey, conducted fourteen and six weeks after these events, respectively, focused on measuring water levels and inundation extents at Hanga Piko and Hanga Roa. All measured levels were confirmed by eyewitnesses and were referenced to MSL by using official harbor drawings provided by the local authority. These drawings include the levels of structures that were captured in the photographs and videos (e.g., gravity quay walls) and therefore served as reference to determine water levels during the events.

4 Sea-level variability at Rapa Nui

The diverse weather phenomena affecting Rapa Nui often induce large sea-level fluctuations at the coast. These are evident in the 17-month-long sea-level time series at Hanga Piko, which shows frequent high-amplitude oscillations that often far exceed the typical high spring tide (Fig. 3d). Together with the wind (Fig. 3b) and waves (Fig. 3c), these high-amplitude oscillations are very likely the main reason behind the frequent harbor shutdowns at Hanga Piko (Fig. 3a).

The spectral separation of the residual sea level shows that both the long- and short-period components contributed significantly to the observed variability (Fig. 3g-h). The contribution of each signal alone is occasionally comparable to, and sometimes even larger than, the maximum high spring tide. This is especially true for the short-period oscillations,

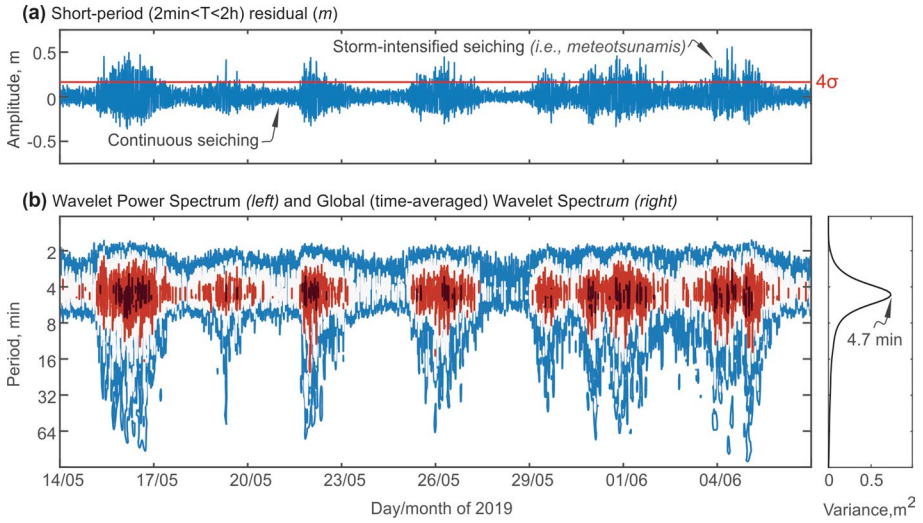

Fig. 4 Continuous and intensified seiching. **a** A 24-day-long segment of the short-period component of residual sea level, between May 14 and June 7, 2019. Red horizontal line indicates four standard deviations (4σ) from the long-term mean shown in Fig. 3h. According to Monserrat et al. (2006), amplitudes exceeding this threshold are defined as meteotsunamis. **b** Wavelet power spectrum (left) and normalized global wavelet spectrum (right) for the time series in (**a**). Reddish colors indicate large energy levels, and bluish colors indicate lower energy levels

whose amplitudes frequently exceed the high spring tide (Fig. 3h). The long-period signal, instead, generally exhibited lower amplitudes but reached significant levels of a few decimeters in late August 2019 and in early March and May 2020 (Fig. 3e). There is a 3-h-data gap in the former event that prevents us from knowing the true sea level reached in that occasion.

A closer examination of the short-period signal reveals the occurrence of continuous seiching off Hanga Piko. This is well illustrated in Fig. 4b which shows the time series and wavelet spectrum between May 14th and June 7th, 2019 (other time windows show similar features). The wavelet spectrum shows that most of the signal variability occurs within a narrow period band centered around ~ 5 min. The reason to believe that these oscillations mainly reflect local seiches instead of other classes of waves (e.g., IG waves) is their roughly constant frequency and persistence, which together strongly suggest that they are controlled by the local submarine and coastal morphology rather than by the properties of the external forcing. Unfortunately, the lack of observations at other sites prevents us from understanding the spatial domain where these seiches occur, but they are very likely occurring on the shelf rather than inside the Hanga Piko Harbor. Indeed, according to the Merian's formula (e.g., Rabinovich 2009), the fundamental or Helmholtz mode of a simplified cross section scaled to the profile shown in the inset of Fig. 1b is 5.5 min, while that for the harbor basin in Hanga Piko is only from a few to several tens of seconds.

Another evident feature of the short-period signal is the frequent intensification of the seiches. This can be seen in Fig. 4, which shows recurrent intensification of the energy around the ~ 5 min period. This pattern clearly resembles the meteotsunami description of Defant (1961), who wrote that *"The Meteorologic tsunami are nothing but seiches of bays and of the shelf, but they exceed in intensity the normally smaller amplitudes of the seiches …"* If we set an amplitude threshold of four standard deviations (4σ), as suggested

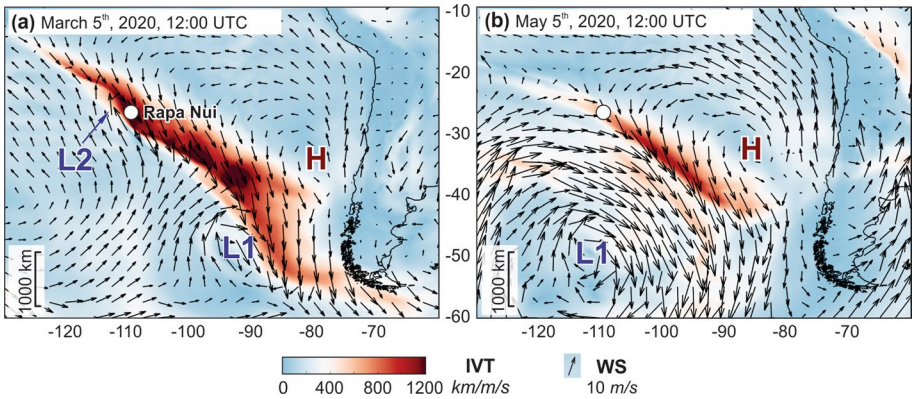

Fig. 5 Synoptic weather conditions during the extreme sea-level events. The arrows represent the wind velocities at 10 m above MSL (see scale at the bottom). Letters H, L1 and L2 indicate the center of the subtropical anticyclone, the midlatitude cyclone and the secondary cyclogenesis, respectively. The white circle is the location of Rapa Nui. The magnitude of the integrated water vapor transport (IVT) is shown in shades (scale at the bottom). **a** is for 12 UTC March 5th, 2020, and **b** for 12 UTC May 5th, 2020

by Monserrat et al. (2006) to define meteotsunamis, we count dozens of seiches that meet this criterion in our 17-month-long analyzed window (Fig. 3h) and therefore fall in the meteotsunami definition of Defant (1961) and others (e.g., Rabinovich 2020). Nonetheless, because we do not clearly understand the external forcing and resonant processes underlying their intensification, we hereafter simply call them intense seiches.

Furthermore, when these intense seiches are accompanied with significant storm surges, the residual sea level increases drastically, and when they both coincide with high tides the water level inside the harbor reaches hazardous levels. During the analyzed period, these hazardous combinations of seiches, storm surges and tides were most extreme during the events of March 5th and May 5th, 2020 (and possibly on the 21 August event). In both occasions, the sea level recorded in the harbor tripled the high spring tide. In the following section, we focus on these two events.

5 The coastal storms of March and May 2020

5.1 Synoptic and local weather conditions

Figure 5 shows the IVT magnitude (background colors) and the wind velocity (arrows) at 10 m above MSL at 12 UTC for March 5th and May 5th, 2020. A salient feature in these maps is a swath of strong NW flow near the surface and high IVT extending for more than 2000 km from the tropical Pacific to midlatitudes, the fingerprint of an AR in this area. The band of strong NW winds extends from the surface to the upper troposphere (not shown) transporting moist air sourced in the tropical central Pacific toward the southeast Pacific. In both snapshots, Rapa Nui was near the major axis of the ARs and we verified that the AR conditions prevailed over the island in a window of about 24 h around those times. The AR of the March event was stronger, wider and longer than that of May, although both reached Category 4 with IVT > 800 kg/m/s, the second strongest according to Ralph et al. (2017). The ARs were ultimately driven by the large-scale pressure gradient between midlatitude

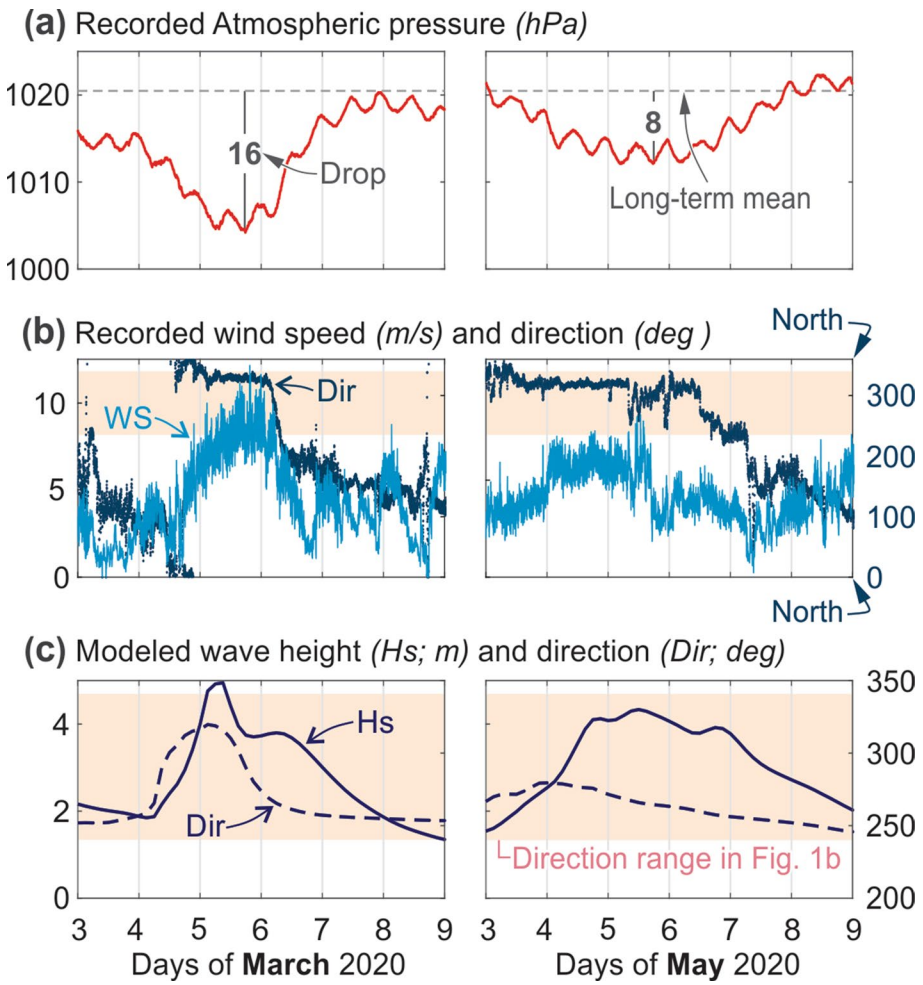

Fig. 6 Local weather and wave conditions during the March 5th (left) and May 5th (right), 2020, extreme sea-level events. Time series of atmospheric pressure **(a)** and wind speed and direction **(b)** recorded at the Mataveri Airport (600 m east of Hanga Piko). **c** Time series of significant wave heights and mean directions modeled at a node located 300 m off Hanga Piko at 20 m water depths (location of the node in Fig. 1b)

cyclones drifting toward southern Chile and the subtropical anticyclone (identified in Fig. 5 as L1 and H, respectively).

To place the two storms in context, the polar diagram of the daily (12 UTC) wind at 27ºS, 109.1ºW (Fig. 2b) includes the wind vector and IVT for March 5th and May 5th, 2020. The March storm stands out for its large IVT value and strong NNW wind, among the largest of the record (~20 m/s). The wind during the May storm was from the NW and accompanied by a large value of IVT. The wind speed was large but not extreme, reaching ~10 m/s on May 5th and ~15 m/s the day before.

The local conditions, recorded at Mataveri airport, indicate some differences between the two storms (Fig. 6a, b). In the first case, the surface wind changed rapidly from near calm on March 3rd to ~10 m/s northerly winds on March 5th (Fig. 6b). In that 36-h period,

the atmospheric pressure dropped by ~10 hPa, influenced by the passage of the main cyclone (L1) at midlatitudes and a secondary cyclogenesis within the AR and very close to Rapa Nui (L2 in Fig. 5a). The absolute atmospheric pressure, however, remained above 1005 hPa, which is not a particularly low value. The atmospheric pressure drop was even weaker for the May event (8 hPa in 48 h), and the wind remained below 8 m/s (except for a brief period on May 5th), but the NNW direction prevailed at least for the 72 h before the highest sea levels were recorded at the tide gauge.

5.2 Wind–wave climate

Our modeled results show large waves with significant heights of up to 5 m and 4.2 m during the March 5th and May 5th events, respectively (Fig. 6c). The March 5th event peaked with NW waves, lasting for about 2 days with wave heights above 4 m (left panel in Fig. 6c). Those during the May 5th event had a roughly constant W direction, remaining with relatively high wave heights for nearly 3 days (right panel in Fig. 6c).

5.3 Visual records and field survey

The effects of both events were partially captured by visual records obtained from eyewitnesses at different locations of the island. These, however, are more abundant for the May event at Hanga Piko. Because the tide gauge is located at this harbor, here we mainly focus on the sea-level fluctuations captured therein.

The May 5th, 2020, event was well captured by one video and two photographs, taken shortly after 23:00 UTC (17:00 local time[2]), only tens of meters away from the tide gauge (Fig. 7). This visual evidence provides lower bound estimates of the peak water levels and flooding extents around the harbor, revealing oscillations that complement the tide gauge record. A striking feature is the clear augmented water level lasting for at least 1 min (length of video), as shown in the left photographs of Fig. 7b-d. By comparing these with photographs taken at the same sites during calm conditions and similar tide levels (~20 cm in both cases), the storm-induced sea levels can be visually inferred. The video also captures intense wave breaking outside the harbor, strong wave agitation induced by waves within the harbor (Fig. 7b) and ubiquitous overtopping around the harbor quay walls (Fig. 7b-d).

In the eastern sector of the harbor, the water level exceeded the quay wall at + 1.4 m above MSL and reached the base of the retaining wall on the other side of the road, which is at + 1.5 m above MSL (Fig. 7b, d). The water level in the southern sector exceeded an even higher quay wall whose crest is at + 1.7 m above MSL (Fig. 7c). We therefore consider + 1.7 m as a lower bound estimate of the maximum runup in this event. Following a similar approach for the March 5th event, we measured water levels of up to + 1.4 m above MSL at both Hanga Piko and Hanga Roa. Although we did not find footage at Hanga Roa for this event, competent witnesses informed that the effects were like those typically produced by regular storms.

[2] Time zones Easter Island: UTC-5 in summer time (September-March) and UTC-6 in winter time (April–August).

Fig. 7 Field survey results and visual effects of the May 5th, 2020, extreme sea-level event at Hanga Piko. **a** Aerial view of the Hanga Piko Harbor and water levels and inundation extents, as derived from video and photographic footage. **b–d** Comparisons of photographs taken at the same site with similar tide levels (0.2 m above MSL) during this event and calm conditions. The left panel of b is a video frame

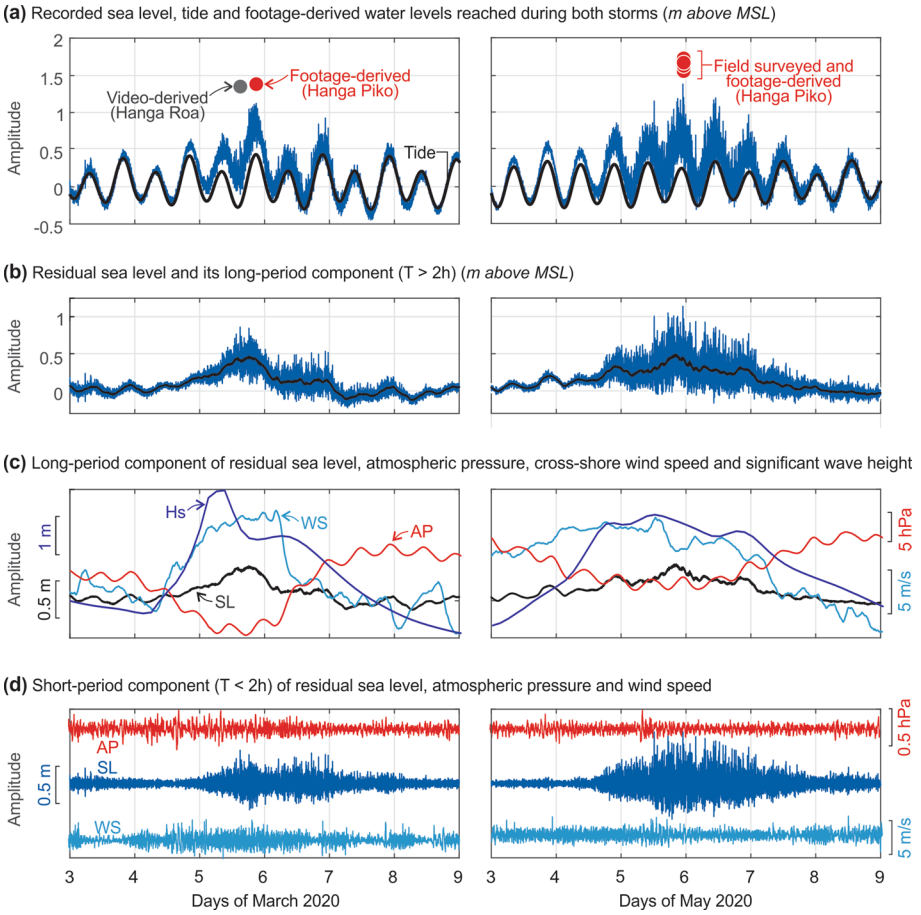

Fig. 8 Time series analysis of the recorded sea level at Hanga Piko during the March 5th and May 5th, 2020, extreme sea-level events. **a** Sea level at Hanga Piko recorded by the tide gauge and inferred from video and photographic footage. **b** Residual sea level (blue) and its long-period component with periods longer than 2 h (black). **c** Comparison of the long-period components of the residual sea level (SL), atmospheric pressure (AP) and cross-shore wind speed (WS), and the modeled significant wave height (Hs). For absolute values, refer to **b** and Fig. 6. **d** Short-period components of the residual sea level (SL), atmospheric pressure (AP) and wind speed (WS). Note that no relevant perturbations occurred in the atmospheric pressure or wind records, which rules out the occurrence of meteotsunamis formed by high-frequency atmospheric perturbations (e.g., Monserrat et al. 2006)

5.4 Time series analysis

Tide gauge records for both events show high-amplitude sea-level oscillations that remained visible for about 3 days (Fig. 8a). Peak levels during the March 5th event occurred at 20:52 UTC (15:52 local time), when the sea level rose up to + 1.1 m above MSL (left panel in Fig. 8a). Although the tide was at its highest level at that moment, its amplitude was only + 0.4 m. In the May 5th event, the highest sea level of + 1.35 m was recorded at 22:51 UTC during a tide of + 0.2 m (right panel in Fig. 8a). Therefore, in both cases, the recorded sea levels were a few decimeters lower than those derived from visual

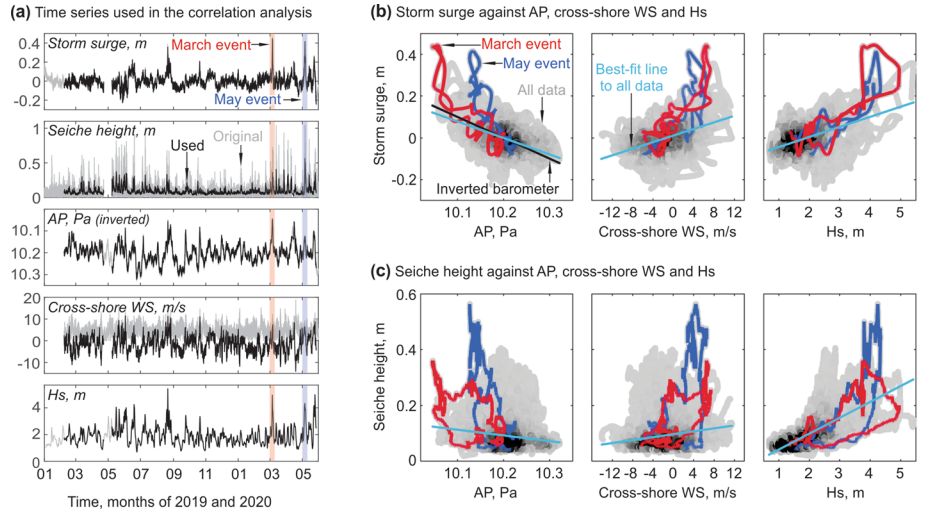

Fig. 9 Correlation analysis between the sea-level signals and the atmospheric and wave datasets. **a** The time series in black are the ones used in the analysis, which are modified versions of the time series in grey presented in Fig. 3 (see text for details) (in the second upper panel, the grey curve is the crest-to-trough heights of the short-period signal of Fig. 3h). **b** Correlation plots between the long-period sea-level residual (storm surge), the atmospheric pressure (AP), cross-shore wind speed (WS) and significant wave height (Hs). For reference, the inverted barometer effect in the left panel is shown by the black line. **c** Same as **b**, but the dependent variable is now the crest-to-trough seiche height, calculated by applying the zero-up crossing method to the short-period sea-level residual shown in Figs. 3h and 8d

records (Fig. 8a). The difference is likely associated with the complex phenomena of wave agitation, harbor resonance and the presence of IG waves which are not captured by the tide gauge due to its relatively low, 1-min sampling interval.

The long-period signal reveals significant storm surges that increased the sea level for 2 days in March and 3 days in May, reaching maximum levels of + 0.5 above MSL in both occasions (Fig. 8b). These, were the highest recorded during the analyzed window, leaving the August 21st (2019) event aside due to the data gap (see Fig. 3g).

The short-period signal reveals intense seiches occurring in both events (blue curve in Fig. 8d). The temporal intensification of these seiches agrees well with the concurring storm surges, with maximum amplitudes of ~ 0.4 m (March 5th, 14:58 UTC) and ~ 0.7 m (May 5th, 22:51 UTC). Therefore, in both events, the extreme water levels inside the harbor are explained by constructive superpositions of high tides, storm surges and intensified seiches, besides shorter-period phenomena captured by the video (Fig. 8a) but missed by the tide gauge.

6 Inferred mechanisms behind the extreme sea levels observed at Rapa Nui

To elucidate the physical processes behind extreme sea-level events, as those observed in March and May, 2020, we performed simple correlation analysis between the sea-level signals and the atmospheric and wind–wave datasets. For this, we considered the time series shown in Fig. 9a, which are modified versions of those in Fig. 3. In particular, we only considered segments with no gaps in all the time series. For the wind speed, we considered the cross-shore components taking 290° as the pure cross-shore direction (Fig. 1b). Also, instead of using the seiche amplitudes, which include both positive and negative values, we used their crest-to-trough heights calculated with the zero-up crossing method. Finally, given that the modeled significant wave heights have 1 data point every 3 h, we smoothed all the time series using a 3-h boxcar window.

6.1 Statistical correlation results

The results for all data show good correlation between the storm surge and the atmospheric and wave data (Fig. 9b). In particular, the storm surge amplitude increases as the atmospheric pressure decreases (i.e., barometric setup) and as both the cross-shore wind speed (i.e., wind setup) and significant wave height increase, which we assume is scaled with the static component of the wave setup. The results also show that the storm surge increase with decreasing atmospheric pressure (represented by the best-fit line to all data) is slightly smaller than what is expected from the inverted barometer effect (compare slopes of the cyan and black lines).

The correlation results for the seiche heights (Fig. 9c) are somewhat different. No clear correlation is observed between this variable and the atmospheric pressure and cross-shore wind speed. A positive correlation, however, is found with the significant wave height, which could be linked to the dynamic component of the wave setup and IG waves generated off the coast of Hanga Piko. As the significant wave heights become larger, the seiche heights increase.

Focusing on the two extreme events of March and May (red and blue lines in Fig. 9), the correlation deviates from the general trend, especially for the seiche height. In particular, regressions feature a greater, and seemingly nonlinear, increase in both the storm surge amplitude and seiche heights when the atmospheric and wave parameters reach extreme values. Although not shown here, this pattern is observed in other extreme events throughout the data. The deviation from the trend in relatively large values, remain to be unexplained in light of the limited sampling frequency of the tide gauge and relatively coarse wave model which does not capture IG waves nor wave agitation in the nearshore.

6.2 Storm surge controlled by both wave and barometric setup

We interpret the correlation results of Fig. 9b as either direct or indirect causal relationships. The increase in the sea level with decreasing atmospheric pressure, or barometric setup, is well known and has been observed in different settings (Wunsch and Stammer 1997), including other volcanic islands (e.g., Kennedy et al. 2012). For the analyzed period, the barometric setup is evident in both the correlation results of Fig. 9b and in

the time series of Figs. 8c and 9a, with a good agreement of storm surge peaks and atmospheric pressure drops.

The positive correlation between the storm surge and the significant wave heights can be explained by the static component of wave setup, which results from the transfer of wave-related momentum to the water column during wave breaking (Pugh and Woodworth 2014). Wave setup has been reported to contribute significantly to elevated water levels especially during severe storms (e.g., Dean and Bender 2006) and can be even larger in regions where the shelf is extremely narrow or inexistent (Kennedy et al. 2012), as it is the case for steep volcanic islands. In the case of Hanga Piko, and according to satellite imagery (e.g., Google Earth), video footage and reports of local dockworkers, waves break a few to several tens of meters from the harbor entrance. Because the tide gauge is located only 50 m from the entrance (Figs. 1b, 7a), it is therefore unusually exposed to wave setup, in contrast to most other tide gauges located in sheltered areas.

The contribution of wind setup to the recorded sea levels is expected to be rather small, in spite of the relatively strong wind speeds and good correlation shown in Fig. 9b. To a first-order approximation, the wind setup scales with the square of the wind speed, it is linearly dependent on the fetch and inversely proportional to the water depth. Despite the large fetch during both events (Fig. 5), the energy transfer from wind to the sea surface occurred over very deep waters. This, plus the very narrow shelf off Hanga Piko, supports a relatively small contribution of wind setup, as previously reported for Rapa Nui (Quillam et al. 2011, 2014) and other volcanic islands (Kennedy et al. 2012).

In summary, from the analysis of meteorological and wave conditions, we posit that extreme storm surges in the March 5th and May 5th, 2020, events were dominated by wave setup, followed by barometric setup, and with little if any contributions of wind setup.

6.3 Seiches on the shelf modulated by wind–wave-related IG waves

Wind-driven phenomena are also the main candidate to explain the short-period sea-level signal. First, given the absence of relevant high-frequency perturbations of atmospheric pressure and wind speed preceding or during the high-amplitude seiches recorded in March 5th and May 5th, 2020 (Fig. 5d), we rule out the atmosphere as the ultimate triggering mechanism of these oscillations (e.g., Monserrat et al. 2006). However, as mentioned in Chapter 4, the seiches with larger than usual amplitudes still fall into the general meteotsunami definition (e.g., Defant 1961), specifically as “bad weather” meteotsunamis (Rabonivoch 2020). Second, given the continuous seiching with a roughly constant period, of ~ 5 min, observed throughout the 17-month-long record, we rule out the continuous occurrence of IG waves, which are expected to have a wider frequency spectrum. Instead, we explain the 5-min oscillations by seiches on the shelf. Given the good correlation with significant wave heights, the amplitude of such seiches is likely controlled, or at least influenced, by the energy transferred from IG waves released during wave breaking to the shelf sea. Whether the seiches are propagating across the shelf or along it as progressive or standing edge waves is not known and needs further investigation.

6.4 The role of atmospheric rivers

Even if the wind did not contribute directly to the enhanced water levels through wind setup, it seemed to play a very important role at least during the March 5th and May 5th extreme events. Indeed, both events occurred during long-lasting (24–48 h) periods of

strong NW winds, a condition that contrasts with the local wind climatology characterized by much weaker easterlies (see Fig. 2b). The local wind conditions were, in turn, associated with strong ARs in which a swath of NW flow and high water vapor transport extended for several hundred kilometers upstream (and downstream) of the island. Thus, we hypothesize that ARs passing over Rapa Nui favor the generation of large NW swells that directly impact the NW facing Hanga Piko Harbor (i.e., little diffraction and refraction). As discussed above, these large waves were the main responsible for augmenting the sea level in both the short- and long-period bands. Although a few studies have reported relations between ARs and high water levels in continental coastlines (Khouakhi and Villarini 2016; Shinoda et al. 2019) via wind setup, what we report here is somewhat different because the phenomena occur on a steep volcanic island surrounded by deep waters where the mechanism is wave setup rather than wind setup. Many issues regarding the connection between ARs and extreme sea levels at Rapa Nui are still unclear for us, but their scientific and societal importance revealed by the observations presented herein motivates their investigation.

7 Concluding remarks

From the analyses of the sea-level record at the main harbor of Rapa Nui (Hanga Piko), located on its western coast, we conclude the following:

1. Beyond the small tidal oscillations, the local sea level is highly variable, with multiple episodes of extreme sea levels. These extreme episodes usually result from the combination of high tides, storm surges and intense seiches on the shelf.
2. Storm surge is dominated by wave setup, followed by barometric setup, and with little if any contribution of wind setup. Seiching is continuous in the records and is very often intensified during intense weather conditions.
3. The two most extreme events during our analyzed period (between January 1st, 2019, and May 31st , 2020) occurred in March 5th and May 5th, 2020, when the sea level in the harbor tripled the high spring tide. Peak levels recorded by the tide gauge were + 1.1 m and + 1.3 m above MSL, respectively, although, according to video footage, real water levels in the harbor were a few decimeters higher.
4. In both cases, Rapa Nui was near the major axis of well-defined atmospheric rivers with a NW–SE direction. We hypothesize that the strong, long-lasting synoptic-scale winds that accompanied both atmospheric rivers favored the generation of large NW swells that directly impacted the NW facing Hanga Piko Harbor, which in turn were the main responsible for increasing the sea level through significant storm surges and intense seiches.
5. Given that the sea level and the strength of atmospheric rivers in the South Pacific Ocean are thought to increase as climate changes (e.g., Espinoza et al. 2018; Dangendorf et al. 2019), a deeper understanding of the meteorological and oceanographic processes affecting the operational efficiency of Rapa Nui's main harbor (and thus its maritime supply chain) is strongly needed.

Acknowledgements This work is dedicated to Lomito. We deeply thank Mauricio Hadida (the Chilean Maritime Governor), Javier Icka Acuña, Felipe Morales Guajardo and Caleb, who provided and discussed the footage analyzed here, and Mauricio Molina and Sebastián Correa for their aid in generating the wave

dataset. We also thank Patricio Catalán, Rodrigo Cienfuegos and Kwok Fai Cheung for fruitful discussions in initial phases of this study, and Roberto Carvajal for connecting us with the local Maritime Authority and for showing us the video that motivated this study. The atmospheric data were provided by the "Dirección Meteorológica de Chile" (http://www.meteochile.gob.cl). The sea-level data were provided by the "Servicio Hidrográfico y Oceanográfico de la Armada de Chile" (http://www.shoa.cl) through the Intergovernmental Oceanographic Commission's sea level station monitoring facility (http://www.ioc-sealevelmonitoring.org/). Wind fields for wave modeling are from NOAA's Global Forecast System GFS database https://www.ncdc.noaa.gov/data-access/model-data/model-datasets/global-forcast-system-gfs. We sincerely thank three anonymous reviewers and Alexander Rabinovich (Guest editor), who, besides providing valuable comments and suggestions to improve our paper, encouraged us to tell the story in a much focused way. PW thanks grant ANID FONDAP 15110017 (CIGIDEN) for the financial support during this study. Funding came from the Iniciativa Científica Milenio (ICM) through Grant Number NC160025 "Millennium Nucleus CYCLO: The Seismic Cycle Along Subduction Zones." and by Chile's Fondo Nacional de Desarrollo Científico y Tecnológico, FONDECYT Projects N°1190258 and N°1181479.

Funding Iniciativa Científica Milenio (ICM) through Grant Number NC160025 "Millennium Nucleus CYCLO: The Seismic Cycle Along Subduction Zones."

Data availability All the used data is provided in the Acknowledgment Section.

Code availability All calculations were done with regular mathematical software.

Compliance with ethical standards

Conflicts of interest There are no conflicts of or competing of interest in this work.

References

Baker PE, Buckley F, Holland JG (1974) Petrology and geochemistry of Easter Island. Contrib Mineral Petrol 44:85–100. https://doi.org/10.1007/BF00385783

Beyá J, Álvarez M, Gallardo A, Hidalgo H, Winckler P (2017) Generation and validation of the Chilean Wave Atlas database. Ocean Model 116:16–32. https://doi.org/10.1016/j.ocemod.2017.06.004

Bilek SL, Lay T (2018) Subduction zone megathrust earthquakes. Geosphere 14(4):1468–1500. https://doi.org/10.1130/GES01608.1

Dangendorf S, Hay C, Calafat FM, Marcos M, Piecuch CG, Berk K, Jensen J (2019) Persistent acceleration in global sea-level rise since the 1960s. Nat Clim Change 9:705–710. https://doi.org/10.1038/s41558-019-0531-8

Dean RG, Bender CJ (2006) Static wave setup with emphasis on damping effects by vegetation and bottom friction. Coast Eng 53(2–3):149–156. https://doi.org/10.1016/j.coastaleng.2005.10.005

Defant A (1961) Physical oceanography, vol 2. Pergamon Press, London, p 613

Espinoza V, Waliser DE, Guan B, Lavers DA, Ralph FM (2018) Global analysis of climate change projection effects on atmospheric rivers. Geophys Res Lett 45(9):4299–4308. https://doi.org/10.1029/2017GL076968

Guan B, Waliser D (2015) Detection of atmospheric rivers: Evaluation and application of an algorithm for global studies. J Geophys Res Atmos 120(24):12514–12535. https://doi.org/10.1002/2015JD024257

Hersbach H de Rosnay P, Bell B, Schepers D, Simmons A, Soci C, Abdalla S, Alonso-Balmaseda M, Balsamo G, Bechtold P, Berrisford P, Bidlot J-R, de Boisséson E, Bonavita M, Browne P, Buizza R, Dahlgren P, Dee D, Dragani R, Diamantakis M, Flemming J, Forbes R, Geer AJ, Haiden T, Hólm E, Haimberger L, Hogan R, Horányi A, Janiskova M, Laloyaux P, Lopez P, Munoz-Sabater J, Peubey C, Radu R, Richardson D, Thépaut J-N, Vitart F, Yang X, Zsótér E, Zuo H (2018) Operational global reanalysis: Progress, future directions and synergies with NWP. European Centre for Medium Range Weather Forecasts. ERA Report Series No. 27. 63 pp.

Kennedy AB, Westerink JJ, Smith JM, Hope ME, Hartman M, Taflanidis AA, Hamann M (2012) Tropical cyclone inundation potential on the Hawaiian Islands of Oahu and Kauai. Ocean Model 52–53:54–68. https://doi.org/10.1016/j.ocemod.2012.04.009

Khouakhi A, Villarini G (2016) On the relationship between atmospheric rivers and high sea water levels along the US West Coast. Geophys Res Lett 43(16):8815–8822. https://doi.org/10.1002/2016GL070086

Monserrat S, Vilibić I, Rabinovich AB (2006) Meteotsunamis: atmospherically induced destructive ocean waves in the tsunami frequency band. Nat Hazards Earth SystSci 6:1035–1051. https://doi.org/10.5194/nhess-6-1035-2006

Liu Y, San Liang X, Weisberg RH (2007) Rectification of the bias in the wavelet power spectrum. J Atmos Oceanic Technol 24(12):2093–2102. https://doi.org/10.1175/2007JTECHO511.1

Pawlowicz R, Beardsley B, Lentz S (2002) Classical tidal harmonic analysis including error estimates in MATLAB using T_TIDE. ComputGeosci 28(8):929–937. https://doi.org/10.1016/S0098-3004(02)00013-4

Pugh D, Woodworth P (2014) Sea-level science: understanding tides, surges. Cambridge University Press, Tsunamis and Mean Sea Level Changes, p 407

Quilliam L, Cox R, Campbell P, Wright M (2011) Coastal climate change impacts for Easter Island in 2100. In Coasts and Ports 2011: Diverse and Developing: Proceedings of the 20th Australasian Coastal and Ocean Engineering Conference and the 13th Australasian Port and Harbour Conference, Engineers Australia, p. 617–622.

Quilliam L, Cox R, Campbell P, Wright M (2014) Coastal climate change impacts for Easter Island in 2100. Rapa Nui J 28(1):60–67

Rabinovich A (2009) Seiches and Harbor Oscillations. In: Kim YC (ed) Handbook of Coastal and Ocean Engineering. World Scientific Publications, Singapore. https://doi.org/10.1142/9789812819307_0009

Rabinovich AB (2020) Twenty-seven years of progress in the science of meteorological tsunamis following the 1992 Daytona Beach event. Pure ApplGeophys 177:1193–1230. https://doi.org/10.1007/s00024-019-02349-3

Rahn D, Garreaud R (2014) A synoptic climatology of the near-surface wind along the west coast of South America. Int J Climatol 34:780–792. https://doi.org/10.1002/joc.3724

Ralph FM, Dettinger MD, Cairns MM, Galarneau TJ, Eylander J (2018) Defining "atmospheric river": How the Glossary of Meteorology helped resolve a debate. Bull Am Meteor Soc 99(4):837–839. https://doi.org/10.1175/BAMS-D-17-0157.1

Rangel-Buitrago N, Contreras-López M, Martínez C, Williams A (2018) Can coastal scenery be managed? The Valparaíso region, Chile as a case study. Ocean Coast Manag 163:383–400. https://doi.org/10.1016/j.ocecoaman.2018.07.016

Rappaport Y, Naar DF, Barton CC, Liu ZJ, Hey RN (1997) Morphology and distribution of seamounts surrounding Easter Island. J Geophys Res: Solid Earth 102(B11):24713–24728. https://doi.org/10.1029/97JB01634

Shinoda T, Zamudio L, Guo Y, Metzger EJ, Fairall CW (2019) Ocean variability and air-sea fluxes produced by atmospheric rivers. Sci Rep 9:2152. https://doi.org/10.1038/s41598-019-38562-2

Tolman H (2014) User Manual and System Documentation of WaveWatch III, Version 4.18. Environmental Modeling Center Marine Modeling and Analysis Branch. 361pp.

Torrence C, Compo GP (1998) A practical guide to wavelet analysis. Bull Am Meteor Soc 79(1):61–78. https://doi.org/10.1175/1520-0477(1998)079%3c0061:APGTWA%3e2.0.CO;2

Viale M, Valenzuela R, Garreaud R, Ralph M (2018) Impacts of Atmospheric Rivers on Precipitation in Southern South America. J Hydrometeor 19:1671–1686. https://doi.org/10.1175/JHM-D-18-0006.1

Wunsch C, Stammer D (1997) Atmospheric loading and the oceanic "inverted barometer" effect. Rev Geophys 35(1):79–107. https://doi.org/10.1029/96RG03037

Affiliations

Matías Carvajal[1,2] · Patricio Winckler[3,4,5] · René Garreaud[6] · Felipe Igualt[7] · Manuel Contreras-López[3] · Pamela Averil[3] · Marco Cisternas[8,2] · Alejandra Gubler[4] · Wolfgang A. Breuer[9]

1 Programa de Doctorado en Ciencias Geológicas, Facultad de Ciencias Químicas, Universidad de Concepción, Concepción, Chile

2 Millennium Nucleus the Seismic Cycle along Subduction Zones (CYCLO), Valparaíso, Chile

3 Escuela de Ingeniería Civil Oceánica, Universidad de Valparaíso, Valparaíso, Chile

4 Centro de Investigación Para La Gestión Integrada del Riesgo de Desastres (CIGIDEN), Santiago, Chile

5 Centro de Observación Marino Para Estudios de Riesgos del Ambiente Costero (COSTAR-UV), Valparaíso, Chile

6 Department of Geophysics and Center for Climate and Resilience Research (CR2), Universidad de Chile, Santiago, Chile

7 Escuela de Arquitectura y Diseño, Pontificia Universidad Católica de Valparaíso, Valparaíso, Chile

8 Instituto de Geografía, Pontificia Universidad Católica de Valparaíso, Valparaíso, Chile

9 Facultad de Arquitectura y Diseño, Universidad Andrés Bello, Viña del Mar, Chile